Journal of Power Sources 450 (2020) 227676

Contents lists available at ScienceDirect

Journal of Power Sources

journal homepage: www.elsevier.com/locate/jpowsour

Efficient synthesis of high-sulfur-content cathodes for high-performance Li–S batteries based on solvothermal polysulfide chemistry

Yu-Ting Weng [a], Hansen Wang [b], Rung-Chuan Lee [a], Ching-Yu Huang [c], Sheng-Siang Huang [a,d], Mozaffar Abdollahifar [a], Li-Ming Kuo [e], Bing-Joe Hwang [e], Chin-Lung Kuo [e], Yi Cui [b,f,**], Nae-Lih Wu [a,d,*]

[a] Laboratory of Energy Materials, Department of Chemical Engineering, National Taiwan University, 106, Taipei, Taiwan
[b] Department of Materials Science and Engineering, Stanford University, Stanford, CA, 94305, USA
[c] Department of Materials Science and Engineering, National Taiwan University, Taipei, 106, Taiwan
[d] Advanced Research Center of Green Materials Science and Technology, National Taiwan University, Taipei, 106, Taiwan
[e] Department of Chemical Engineering, National Taiwan University of Science and Technology, Taipei, 106, Taiwan
[f] Stanford Institute for Materials and Energy Sciences, SLAC National Accelerator Laboratory, California, 94025, USA

HIGHLIGHTS

- Facile and efficient synthesis of high-sulfur-content S–C composite is reported.
- The process is based on a novel solvothermal polysulfide chemistry in NMP.
- Efficient infiltration of S into C arises from strong polysulfide-C coupling.
- Composite powders with S contents up to 90 wt% are successfully synthesized.
- The resultant composite cathodes exhibit outstanding rate and cycle performance.

GRAPHICAL ABSTRACT

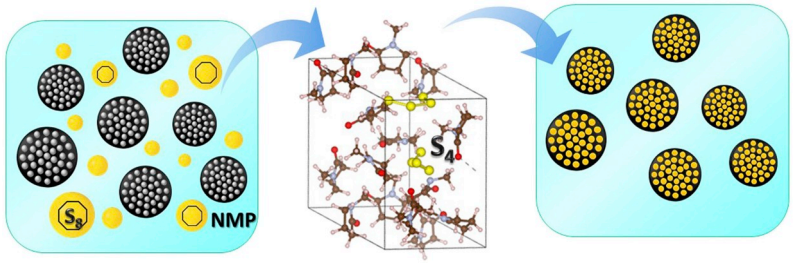

ARTICLE INFO

Keywords:
Lithium-sulfur battery
High sulfur content cathode
High loading electrode
Solvothermal polysulfide chemistry

ABSTRACT

A novel solvothermal polysulfide (PS) chemistry enables a facile and highly efficient process for synthesizing sulfur-carbon (S–C) composite powders containing up to 90 wt% S for high-performance Li–S batteries. Molecular dynamics calculations and experimental analyses reveal the formation of PSs upon dissolution of elemental S in N-methyl-2-pyrrolidone (NMP) at elevated temperatures and efficient infiltration of the PSs into the carbon host driven by the strong coupling with the C surfaces. The coupling enables extensive contact between S and C in the composite, leading to promising electrochemical properties for Li–S battery applications. In the power-type configuration, the composite cathodes having medium-to-high S contents (55 and 75%) demonstrate stable capacity at high current densities up to 100C (1C = 1670 mA g^{-1}-S) and no capacity fade up to 1000 cycles at 2C. In the energy-type configuration, a high-S-content and high-loading (90%-S, 4.2 mAh cm^{-2}) cathode shows a specific capacity of 1440 mAh g^{-1} (86% S utilization) and 90% capacity retention after 300 cycles. This synthesis method enables significant advancement in realizing large-scale applications of Li–S batteries.

* Corresponding author. Laboratory of Energy Materials, Department of Chemical Engineering, National Taiwan University, 106, Taipei, Taiwan.
** Corresponding author. Department of Materials science and Engineering, Stanford University, Stanford, CA, 94305, USA.
E-mail addresses: yicui@stanford.edu (Y. Cui), nlw001@ntu.edu.tw (N.-L. Wu).

https://doi.org/10.1016/j.jpowsour.2019.227676
Received 29 October 2019; Received in revised form 23 December 2019; Accepted 29 December 2019
Available online 5 January 2020
0378-7753/© 2020 Elsevier B.V. All rights reserved.

1. Introduction

The lithium–sulfur (Li–S) battery has attracted widespread attention as a promising energy storage device because of its outstanding theoretical storage capacity of 1672 mAh g^{-1}-S and specific energy of 2.6 kWh kg^{-1}-Li_2S. More importantly, sulfur is naturally abundant, inexpensive, and environmentally benign [1–4]. Li–S batteries thus have considerable potential for applications in large-scale energy storage. Both the initial S cathode and the lithiated end-product, Li_2S, are electrically insulating. For overcoming this problem, it has been a common practice to use nanostructured conductive carbon (C) materials as the S-hosting conductive network [5–9]. However, high-surface-area carbon materials typically have low density, which may lead to low energy density of the electrode as a whole. Increasing the S content in the S–C composite cathode is therefore imperative for achieving high energy and capacity densities.

For achieving high energy density for Li–S batteries, two terms, including high-S-loading (HSL) and high-S-content (HSC), have been brought up in the literature. Although both terms favor the attainment of high energy density, they fundamentally address different issues. As illustrated in Scheme 1, the current collector in a battery plays the role of providing a low-resistance pathway to electric current throughout a battery. While being indispensable for large-format batteries, the current collector is electrochemical inactive, and its presence is at the cost of the energy density of a battery. The HSL concept is meant to dilute the "dead volume" effect of the current collector by increasing the capacity, i.e., the amount of S for Li–S batteries, per unit area of the electrode, as illustrated by Schemes 1a and b. However, if the S content of the composite particle is low, one requires a large quantity of the composite particles in order to fulfill the designated capacity loading. As a consequence, the energy density of the electrode remains low (Schemes 1c and d). To truly accomplish high energy density of the electrode, one needs to employ the HSC composite particles to reduce the total volume of the active layer for achieving the same capacity loading (Scheme 1e). Although there has been a vast number of reports investigating HSL cathodes (areal capacity loading $\geq$4mAh cm^{-2}) [10–15], research on the synthesis of HSC (S content $\geq$80 wt%) particles is substantially less.

The melting–infiltration (MI) method, in which S is melted under vacuum and infiltrates a porous C host through capillary action, has most commonly been adopted for synthesizing S–C composite cathode materials directly from low-cost elemental S (S_8) [16–18]. Nevertheless, the MI process is time-consuming because of slow diffusion of molten S, and typically results in a S content no greater than around 60 wt%. Higher S contents result in S agglomerates ouside the C particles. On the other hand, Cheng et al. [19] synthesized a HSC (90 wt% S) material by ball-milling a mixture of C nanotubes and S particles. Du et al. [20] prepared a HSC material using an antisolvent process. Both cases took the advantage of low-cost elemental S, but gave insufficient electrochemical performance (for example, specific capacities less than 800 mAh g^{-1} at 0.1C). HSC cathode materials have also been obtained through solution redox routes [21–24] in which Na_2S or NaS_2O_3 were subjected to oxidation/reduction to produce zero-valent S. However, the starting salts are considerably more expensive than elemental S, and costly purification steps are required to minimize contamination of chemical residues, including oxidants and acids, which readily deteriorate the performance of the battery system. A combination of inexpensive raw materials and a simple process for manufacturing battery electrodes is highly appreciated in the context of reducing the cost of energy storage in large-scale applications. In this paper, we demonstrate a facile and efficient process that, based on a novel solvothermal polysulfide chemistry (SPC), enables the use of elemental S as the raw material for synthesizing composite cathodes with S contents up to 90 wt% and outstanding specific capacity and cycle stability.

2. Experimental

2.1. Synthesis of S–C composite powders

To synthesize the S–C composite particles, reaction solutions were prepared using different mass ratios between carbon black (CB; BLACK PEARLS® 2000, Cabot) and S powder (99.98%, Aldrich)—0.45:0.55, 0.35:0.65, 0.25:0.75, and 0.1:0.9—and by using N-methyl-2-pyrrolidone (NMP, C_5H_9NO) as the solvent. The solutions, with a solid-to-liquid weight ratio of 1:10, were placed in sealed containers and heated to 180 °C in an oil bath with constant stirring for 2 h, after which they were naturally cooled to room temperature. The powders were collected through filtration, washed with ethanol, and finally dried at 50 °C for 12 h. In one experiment, ethanolamine (ETA, C2H7NO), instead of NMP, was used to prepare the composite powder with an initial CB:S ratio of 0.1:0.9 and a heating temperature of 160 °C.

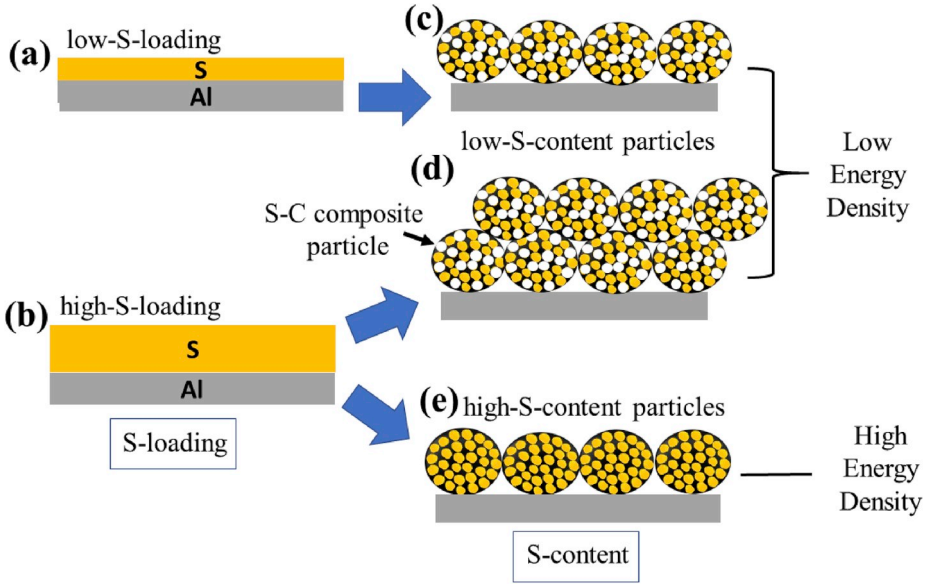

Scheme 1. Schematic elucidating the difference between high-sulfur-loading (HSL) and high-sulfur-content (HSC) concepts. (a)-(b) HSL addresses diluting the "dead volume" contribution of a current collector by increasing the active-material (S) loading per unit area of electrode; (c)-(e) HSC addresses reducing the unfilled pores within the S–C cathode particles. High-energy-density cathode can only be achieved by simultaneously taking into account of HSL and HSC, as shown in (e).

2.2. Material characterization

Microstructural characterization was conducted using scanning electron microscopy (SEM; JSM-7600F, JEOL) and transmission electron microscopy (TEM; FEI Tecnai TF20, Philips). Pore size distributions were determined through Barrett–Joyner–Halenda (BJH) analysis of N_2 adsorption (Micromeritics ASAP 2020). Powder X-ray diffraction (XRD) was performed using a diffractometer (X-pert/Philips) with Cu K_α radiation. Surface analysis was carried out using X-ray photoelectron spectroscopy (XPS, Thermo Scientific, Theta Probe). Thermogravimetric analysis (TGA) was conducted on Rigaku Thermo Plus 2 TG8120 system at temperatures from 30 °C to 1000 °C at 5 °C min^{-1} in an air atmosphere with a sample loading of 10 mg.

2.3. Electrochemical measurements

The working electrodes were prepared by mixing 75 wt% S–C nanocomposite, 13 wt% conductive additives (multiwall carbon nanotubes and super P), and 12 wt% poly-vinylidene-fluoride (PVdF) in NMP to form a homogenous slurry, which was then coated onto an aluminum foil having a graphitic coating layer. The slurry was then dried at 50 °C for 24 h in a vacuum oven. To test the electrochemical properties, 2032-type coin cells were assembled in an argon-filled glove box with Li foil as the counter electrode. In some cases (for 90%-S cathode), a carbon interlayer (~2 μm thick) between the cathode and separator was used. The electrolyte, in an amount of around 10 μL g^{-1}-S−C, was 1.0 M lithium bis(trifluoromethane-sulphonyl)imide ($LiN(SO_2CF_3)_2$, LiTFSI; 99.95%, Aldrich) in a mixture solvent of 1,3-dioxolane (DOL; 99.8%, Aldrich) and 1,2-dimethoxyethane (DME; 99.5%, Aldrich) (DOL:DME = 1:1, v/v) either with or without 3 wt% $LiNO_3$. Galvanostatic charge–discharge test was performed using a cutoff voltage range of 1.5–2.8 V (1.7–2.8 V when $LiNO_3$ is added) (vs. Li^+/Li) with the MCN6410 Arbin battery testing system. Specific capacity is expressed on the basis of the mass of S.

2.4. Computation

All atomic structures, energetics, and electronic properties reported herein were calculated using density functional theory within the generalized gradient approximation and with the Perdew–Burke–Ernzerhof parametrization [25] for the exchange-correlation functional. Computations were performed using the Vienna *ab initio* simulation package [26]. The valence electron wave functions were expanded in plane-wave basis sets, and the projector augmented wave (PAW) method was used to describe the core–electron interactions. The plane-wave cutoff energy was set to 550 eV for both the geometric optimization and electronic property calculations, whereas a cutoff energy of 400 eV was used for *ab initio* molecular dynamics (AIMD) simulations. For Brillouin zone sampling, only the Γ point was used in the AIMD simulations, and a $3 \times 3 \times 3$ *k*-point mesh in the Monkhorst–Pack scheme was employed in the geometric optimization and electronic property calculations. During the AIMD simulations, the equation of motion was integrating using the Verlet algorithm with a time step of 1 fs, and the Nosé–Hoover thermostat was employed to control the temperature of the simulated system.

3. Results and discussion

S–C composite powders with designated sulfur contents ranging from 45 to 90 wt% were successfully prepared by the SPC process. In all cases, the synthesis method demonstrated an extremely high efficiency (within 1 wt% difference) in recovering the S initially introduced into the solution (Fig. 1 and Fig. S1 in SI). As an example, when a powder mixture with a S:CB weight ratio of 9:1 was initially introduced in the solution, the resultant composite powder had a S content of 89.2 wt% (Fig. 1a). (Because of the very small differences between the designated S compositions and the resulting S contents, for simplicity, the composite powders will hereafter be referred to according to the designated S content.) The specific surface area and pore volume were dramatically reduced from 1364 $m^2 g^{-1}$ and 3.5 $cm^3 g^{-1}$ for the initial CB to 9.0 $m^2 g^{-1}$ and 0.08 $cm^3 g^{-2}$ (Fig. 1b), respectively, for the final composite. The dramatic reduction in the pore volume indicates that S efficiently infiltrates and occupies the pores within the CB particles. The resulting S in the CB particles was in crystalline form (Fig. 1c). SEM analysis revealed granular morphology (Fig. 1d) of the composite powder resembling that of the initial CB powder (Fig. S2a) with no observation of S agglomerate on the C surfaces. This is also true for all the synthesized powders with other S contents (Figs. S2b–e). Based on the BJH pore-volume data, it is estaimated that for the 90 wt% S powder less than 3% S could be outside the pores, and this small portion of S is believed to exist as a coating on the particle surface in view of the SEM results. TEM analysis was carried out on the pristine CB particles and the composite particles with 90 wt% S (Fig. S3). The pristine particle showed fringes of C layers within the outer shell region and tortuous pores in the interior. These features could no longer be seen after the pores were filled with S.

Fig. 2 compares the pore size distributions derived from N_2 adsorption isotherms for the MI and SPC S–C composite powders, revealing the fundamental difference in the nature of S infiltration process in these two synthesis methods. For the 45 wt% SPC composite powder, the pore volume was found to contrinuously decrease with decreasing pore size. With further increase in S content, smaller pores dimished at a faster pace than the large pores. This trend suggests that the S-containing species in the SPC method can easily access to the micro-and meso-pores within the particle to preferntially deposit sulfur therein. In contrast, the 45 wt% MI composite exhibted a rise in unfilled pores smaller than 5 nm, suggesting that the S melt has difficulty in getting into these smaller pores.

In order to observe the state of S during the heating process, an experiment was conducted by heating the S particles in NMP without the presence of CB (which would otherwise turn the solution black from the beginning). It was observed that S was completely dissolved at approximately 60 °C and the solution subsequently exhibited color change from being clear to orange and finally to dark black when the solution was continuously heated up (Fig. S4). Upon cooling, shiny yellowish particles—later confirmed through XRD to be highly crystalline sulfur particles—were precipitated (Fig. S4d). The formation of S crystallites as the end-product was consistent with the results for the SPC 90% composite (Fig. 1c), except that in the composite, the crystallites were produced inside the pores of the carbon host. The appearance of the black color of the solution after prolonged heating may be due to the formation of S dye. Black S dyes may be produced by sulfurization of organic species containing nitro and amino groups [27]. However, such reactions cannot proceed to any significant extent without catalysts. In the present experiment, the solid-to-NMP ratio is 1:10 and less than 1% S was lost. This amounts to no more than 0.3% NMP molecules sulfurized. Therefore, the S dye formation is not expected to play any significant role in the process. Indeed, as shown later, there is no correlation between achieving high S content and solution blackening. Attempt to carry out spectroscopy analysis on the state of sulfur in the solution during various stages of heating turned out to be unsuccessful, because sulfur always precipitated out of the solution when the solutions were cooled down to room temperature for the intended analysis.

Theoretical calculations were thus performed in order to reveal potential interactions among S molecules (S_8), NMP, and carbon particles. A*b initio* molecular dynamics (AIMD) simulation revealed that NMP can have the HOMO level higher than the LUMO of S_8 at elevated temperatures, leading to electron charge transfer to S_8. S_8 molecules gain partial electron charge from the surrounding NMP molecules to become ring-opened and decomposed to form negatively charged polysulfides (PSs) with various lengths, stabilized by positively charged surrounding NMP molecules. The formation of the PSs may partly explain the observed color changes of the solution during heating [28] (Fig. S4b).

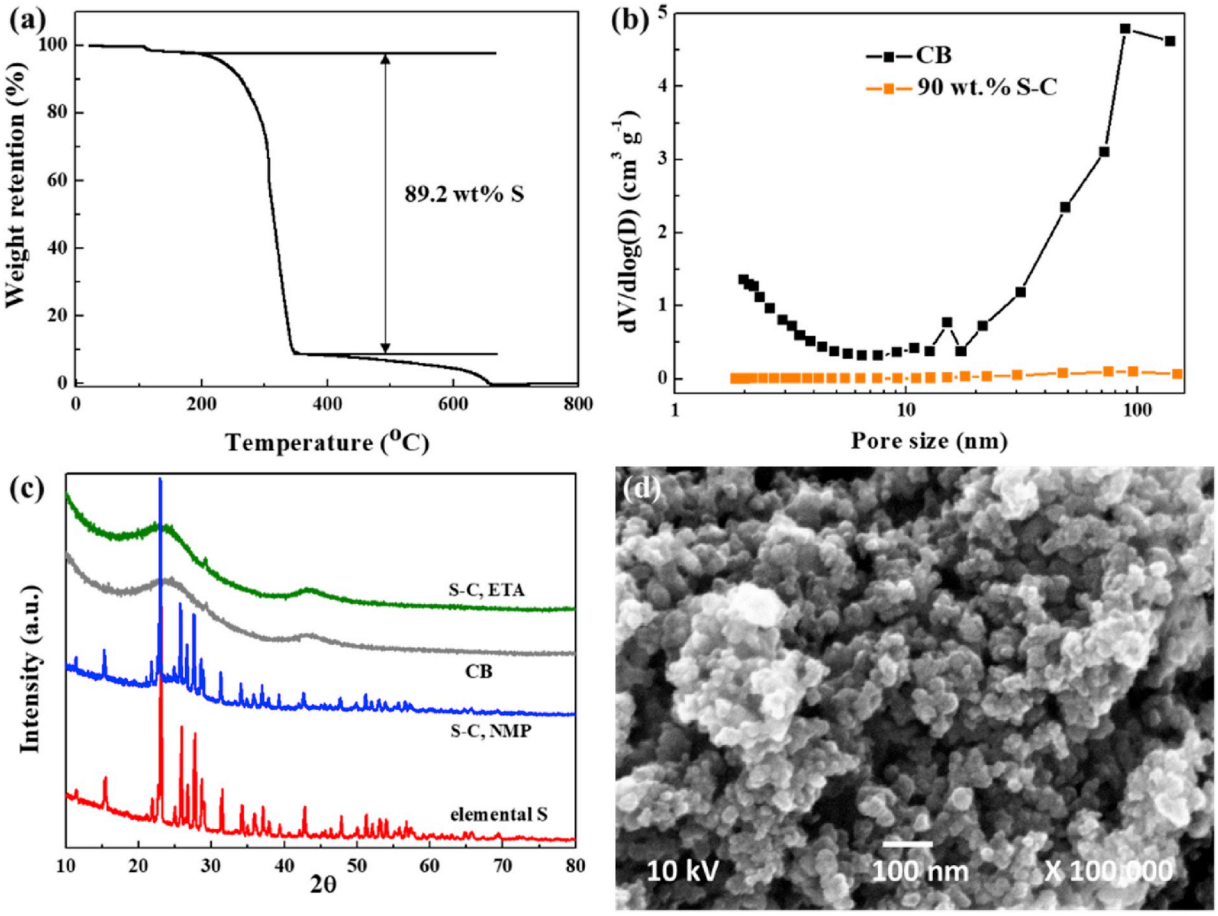

Fig. 1. Material characterizations of the SPC_90% S composite powder: (a) thermogravimetric analysis; (b) pore size distribution using nitrogen adsorption; (c) XRD patterns; (d) SEM micrograph.

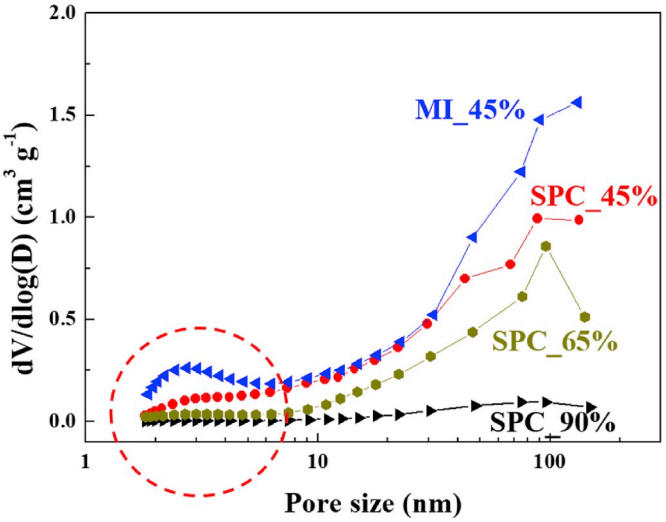

Fig. 2. N_2 adsorption isotherms for a S–C composite powders synthesized by the MI process with a S content of 45% and powders by the SPC process with a S content of 45%, 65% and 90%, respectively. The dashed circle highlights the difference in the filling efficiency of S in smaller pores.

Fig. 3a, for example, displays a snapshot of a S_8 molecule placed in a supercell containing NMP molecules in a 5.0-ps simulation, showing decomposition of the molecule into two S_4 fragments. Fig. 3b displays the charge density difference associated with the decomposition, showing electron charge gain by the S_4 fragments as opposed to the loss by the NMP molecules.

Calculation further revealed that when the S_4 fragment surrounded by NMP molecules comes into contact with a graphene layer (Fig. 3c), which represents the surface of the carbon particle, the NMP molecules undergo reduction by gaining partial electron charge from the graphene surface (i.e., passing the positive charge to the graphene surface), whereas the S_4 fragment remains unchanged (retains its negative charge). These charge transfer processes eventually lead to enhanced adsorption of the PS fragments on the carbon surface due to the electrostatic attraction between them. Calculations of the adsorption energy of a S_4 fragment on a graphene layer, for example, revealed an adsorption energy of −0.19 eV per sulfur atom of S_4, which is 0.13 eV greater than that of a neutral S_8 ring molecule (−0.06 eV).

In a separate experiment, a S–C composite powder with a designated S content of 90% was synthesized by filtrating the dispersion solution immediately at the end of the heating. The "quenched" composite showed a S content of 54%, indicating that a very large portion of the PS fragments were already inside the pores even at high temperatures, supporting the notion of strong PS-C coupling. The results also suggest that S, in the form of PSs, continued to permeate the porous carbon host during the cooling period.

Based on the theoretical calculations and experimental observations described above, it is inferred (Scheme 2) that the carbon particles act as a sink for the PS fragments and are filled with a high concentration of PS fragments at elevated temperature. During cooling, the fragments inside the pores recombine because of oversaturation to form S_8 crystallites. Because of the high concentration of PS fragments inside the pores, S_8 precipitation occurs therein at a much earlier stage than in the bulk

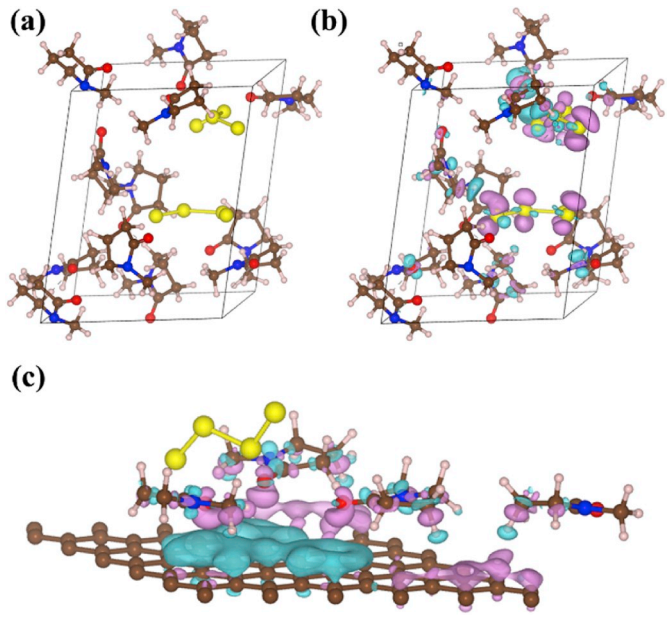

Fig. 3. AIMD simulation: (a) snapshot of a S_8 molecule in NMP, showing cleavage of S_8 into two S_4 fragments (element presentation: red: O; royal blue: N; brown: C; white: H; yellow: S); (b) charge density difference after S_8 fragmentation in NMP, showing isosurfaces representing the gain (loss) of electron charge in violet (light blue); (c) charge density difference when a S_4 fragment surrounded by NMP molecules comes into contact with a graphene monolayer (color presentation is the same as that in b), indicating that the graphene surface loses partial electron charge to the NMP molecules, whereas the S_4 fragment is unchanged (retains its negative charge). (For interpretation of the references to color in this figure legend, the reader is referred to the Web version of this article.)

solution. The consumption of the PS fragments inside the pores draws a constant flux of PS fragments from the bulk solution into the pores, resulting in highly efficient S infiltration.

To further elucidate the important role of the PS formation in realizing the HSC composite, an experiment of using ethanolamine (ETA), instead of NMP, as the solvent was conducted for comparison. Although ETA having the same constituent elements as NMP, the AIMD simulation indicated that the HOMO level of ETA is lower than the LUMO of S_8 even at elevated temperatures, and therefore no electron charge transfer is expected to occur between ETA and S_8. The calculation showed that S_8 molecule was not fragmented in ETA solvent even when equilibration was performed with a long simulation time (Fig. S5a). When following the same procedure as that for preparing the 90% S–C composite in NMP, the process using ETA produced a S–C composite powder containing merely 24% S (Fig. S5b). The poor S infiltration in ETA may result because S_8 molecules, unlike PS fragments, do not have a strong tendency to be adsorbed on the surface inside the pores of the CB particles. These results support the notion that PS formation plays an important role in enabling efficient S infiltration into a porous carbon host in the SPC process. It is worth mentioning that solution of ETA containing S also turned black after prolonged heating. Therefore, there is no correlation between achieving high S content and the black S dye formation in the bulk solution.

Fig. 4 presents the X-ray photoelectron spectroscopy (XPS) spectra acquired from an SPC composite sample. In the S 2p spectra (Fig. 4a), other than the two high peaks at 165 and 164 eV, which can be respectively assigned to $2p_{1/2}$ and $2p_{3/2}$ of zero-charge S (S^0), the broad peak at 162–163 eV indicates the presence of negatively charged PS (S_n^-) species [29], which are believed to originate from the PS fragments adsorbed on the carbon surface. The C 1s spectrum (Fig. 4b) exhibits a high peak at 284.6 eV, which is typical of zero-charge C, and the tail toward high binding energy is associated with more positively charged C species. The high-energy tail can be attributed to the combination of C–N, C–O, and C^+–S^-. The C–N and C–O are believed to arise from NMP residue, whereas the C^+–S^- may be related to the PS adsorption on the carbon surface.

The electrochemical performance of the SPC derived powders were assessed in two configurations. In the "power-type" configuration, the cathodes made of the powders with medium S contents, 55 wt% and 75 wt%, were tested in coin cells containing a Li foil as the anode, a blank separator (without C interlayer) and no $LiNO_3$ in the electrolyte (as described in the Experimental section, all the cathodes contain 13% C

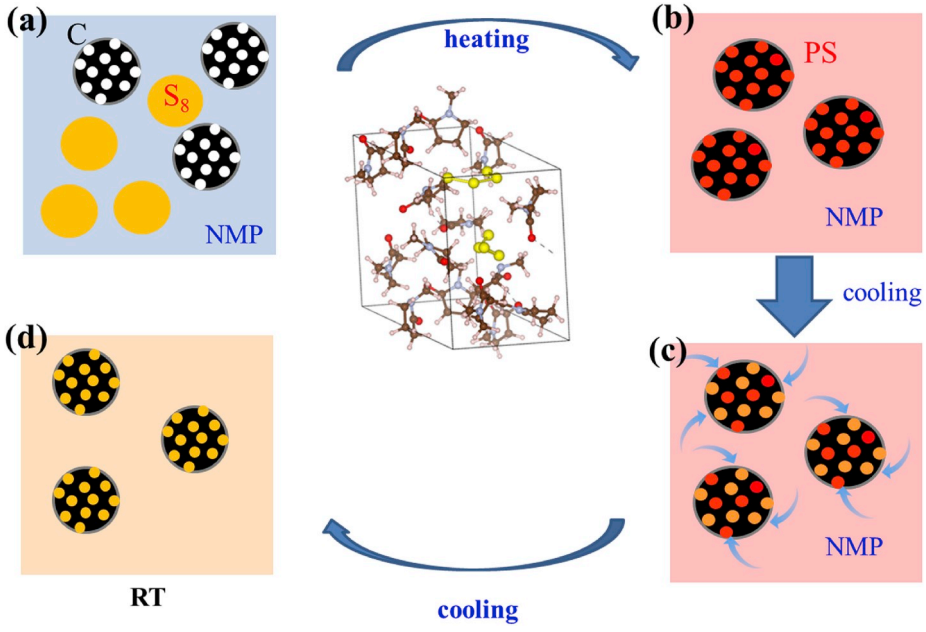

Scheme 2. The proposed SPC process for S infiltration into porous carbon, including (a)→(b) formation of PS upon heating to elevated temperature; (b)→(c) preferential crystallization of S within the particles to draw PS flux into the particles upon cooling; and (c)→(d) finally the formation of S–C composite powders of high S-contents.

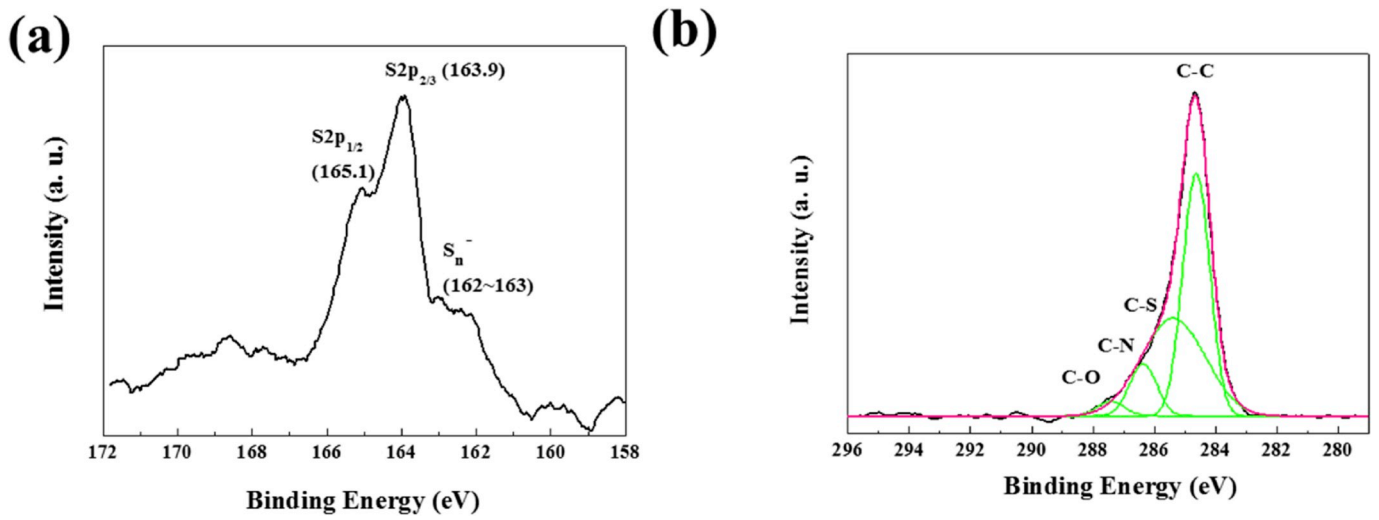

Fig. 4. XPS spectra of the S–C composite prepared by the SPC process: (a) S_{2p}; (b) C_{1s} spectra.

conductive additives). Both electrodes demonstrated exceptional high-current capability. As shown in Fig. 5a and b, the 55%-S electrode showed a stable specific capacity of 1103mAh g^{-1} at 0.2C (all the specific capacity data are expressed on the basis of the mass of S; 1C = 1670 mA g^{-1}-S) and 606 mAh g^{-1} at 10C, and continued to deliver stable capacities of 500–100 mAh g^{-1} with increasing current density from 20 up to 100C. To our knowledge, stable capacities at such high current densities are unprecedented for Li–S batteries. The strong S–C coupling resulting from the SPC process enables extensive and close contact between the conductive C host and embedded S so that the S can efficiently be utilized even under high current rates. It is worth mentioning that the use of a graphitic coating layer on the Al current collector (see

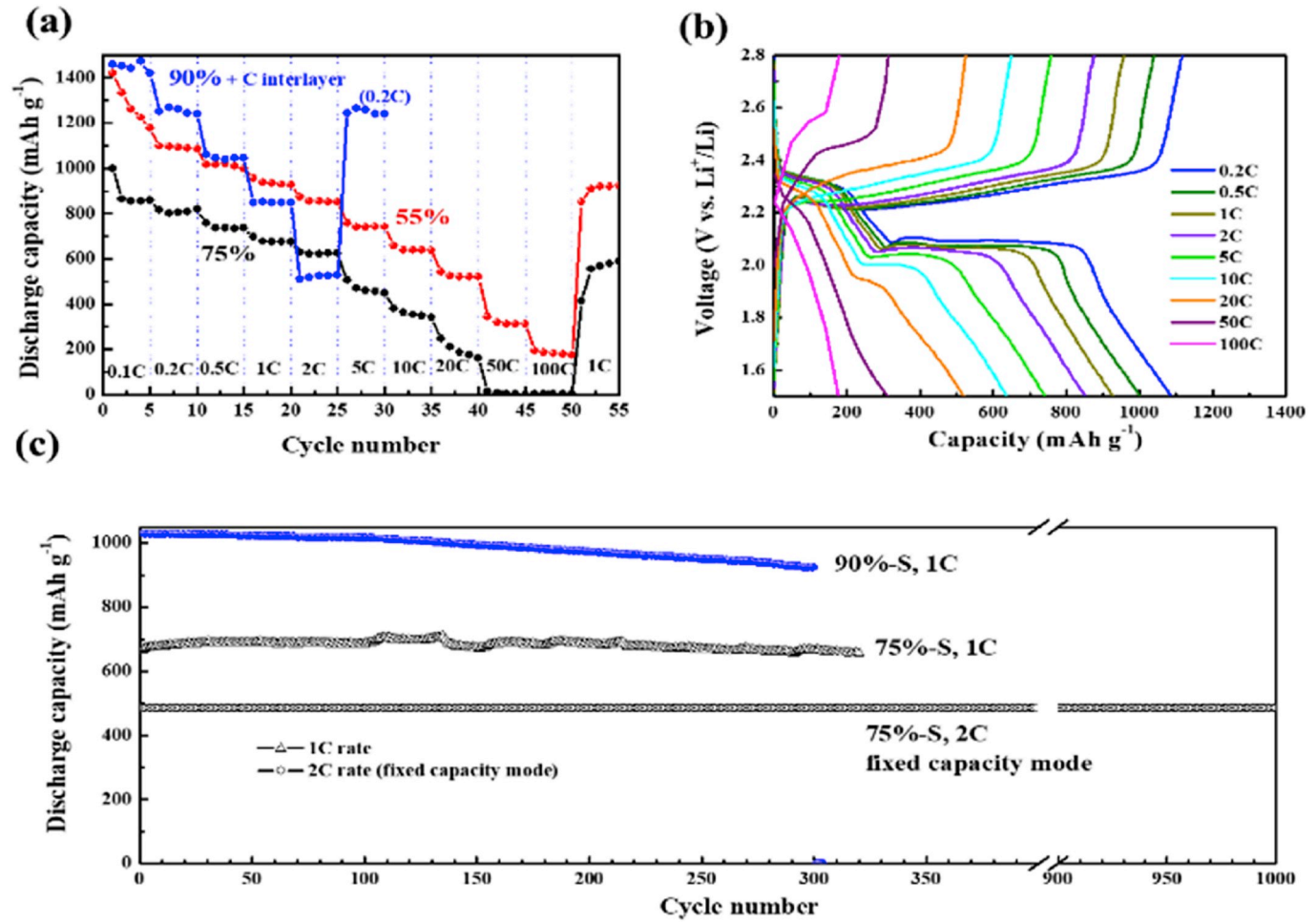

Fig. 5. Electrochemical characterization: (a) specific capacity versus current rate for 55%, 75%, and 90%-S electrodes; (b) charge–discharge voltage curves of 55%-S cathode shown in (a); (c) cycle performance for 75%-S electrode (under two conditions) and 90%-S electrodes.

Experimental) was also found to benefit rate performance.

The 75%-S electrode, exhibiting a specific capacity of 850 mAh g^{-1} at 0.1C, was capable of delivering a specific capacity of 450 mAh g^{-1} at 20C (Fig. 5a). Moreover, the cell showed essentially no capacity loss after 400 cycles when cycled at 1C over a full capacity range or 1000 cycles at 2C with a fixed 80% discharge capacity (approximately 500 mAh g^{-1}) (Fig. 5c).

The cathode made of the powder with a S content of 90 wt% was tested for the "energy-type" configuration. With increasing areal S loading of the electrode, dissolution and shuttling of PSs in the cell resulted in enlarging capacity loss during the initial cycles. To remedy this problem, the 90%-S electrode was characterized in the cell that employed a C interlayer between the cathode and the separator, along with the addition of 3 wt% $LiNO_3$ in the electrolyte. As shown in Fig. 5a, the 90%-S cathode delivered a stable specific capacity of 1440 mAh g^{-1} (0.1C), corresponding to a S utilization ratio of 86%, and an areal capacity of 4.3 mAh cm^{-2} (surfur loading of 3.0 mg cm^2). This electrode may be considered to fulfill the criteria for both HSL ($\geq$4 mAh cm^2) and HSC ($\geq$80 wt%). Its specific capacity was essentially the same as that of a 55% S–C cathode prepared by the same (SPC) method, but substantially higher than that of the MI 55% S–C cathode (Fig. S6). It is also considerably higher than those ($\leq$800 mAh g^{-1}) of previously reported 90% S–C cathodes made using elemental S particle precursor [19,20] and rivals those of the cathodes adopting the solution redox routes [21–24]. The SPC solution method, nevertheless, is considerably simpler and potentially more cost-effective than the solution redox routes. Furthermore, the 90%-S cathode was able to achieve promising charge/discharge rate performance and cycle stability. The electrode retained a specific capacity of 1030 mAh g^{-1} at 0.5C (Fig. 5a) (for voltage curves at different C-rates, see Fig. S7), and retained 90% capacity after 300 cycles. The high surfur utilization and outstanding rate capability and cycle stability exhibited by the SPC S–C cathodes may benefit from the close contact between the conductive carbon host and the embedded sulfur enabled by the strong PS-C coupling.

In summary, a facile synthesis method was developed based on a novel PS chemistry for preparing HSC composite cathodes for Li–S batteries. This process employs inexpensive elemental S as the starting material and involves a simple solvothemal procedure. Theoretical calculations and experimental analyses indicated that the high efficiency of S permeation into the C host was driven by the formation of PSs in NMP at elevated temperatures and strong coupling between the PSs and extensive surface inside the pores of the C host. The strong S–C coupling resulted in enhanced electrochemical performance. Composite cathodes having a medium-to-high S content (55 and 75%) exhibited exceptional rate capability and cycle stability. Moreover, the 90%-S cathode delivered a specific capacity of 1440 mAh g^{-1} (equivalent to a Sutilization of 86%) and an areal capacity of 4.2 mAh cm^{-2} with 90% capacity retention after 300 cycles.

The SPC method greatly simplifies the process for synthesizing HSC cathode powder, which we believe is crucial for realizing large-scale applications of Li–S batteries. For sclaing up the process, however, it should be pointed out that measures (such as using steanless-steel container) should be taken to minimize the NMP loss through evaporartion. Furthermore, the potential adverse effect of NMP sulfurization on the S recovery efficiency upon NMP reusage should be assessed.

Declaration of competing interest

The authors declare that they have no known competing financial interests or personal relationships that could have appeared to influence the work reported in this paper.

Acknowledgements

This work is financially supported by the "Advanced Research Center for Green Materials Science and Technology" from The Featured Area Research Center Program within the framework of the Higher Education Sprout Project by the Ministry of Education (108L9006) and the Ministry of Science and Technology in Taiwan under the grants of MOST-108-3017-F-002-002, and also of MOST-107-2221-E-002-106-MY3, -108-2119-M-002-010, -107-2923-E-011-002, -108-3116-F-301-001-F. The authors also thank Ms. S. J. Ji and Ms. C. Y. Chien (MOST; NTU) for their assistance in performing electron microscopy analyses.

Appendix A. Supplementary data

Supplementary data to this article can be found online at https://doi.org/10.1016/j.jpowsour.2019.227676.

References

[1] P.G. Bruce, L.J. Hardwick, K.M. Abraham, Lithium-air and lithium-sulfur batteries, MRS Bull. 36 (2011) 506–512.
[2] M. Wild, L. O'Neill, T. Zhang, R. Purkayastha, G. Minton, M. Marinescu, G.J. Offer, Lithium sulfur batteries, a mechanistic review, Energy Environ. Sci. 8 (2015) 3477–3494.
[3] R. Van Noorden, The rechargeable revolution: a better battery, Nature 507 (2014) 26–28.
[4] P.G. Bruce, S.A. Freunberger, L.J. Hardwick, J.M. Tarascon, Li–O_2 and Li–S batteries with high energy storage, Nat. Mater. 11 (2012) 19–29.
[5] G. Zhou, J. Sun, Y. Jin, W. Chen, C. Zu, R. Zhang, Y. Qiu, J. Zhao, D. Zhuo, Y. Liu, X. Tao, W. Liu, K. Yan, H.R. Lee, Y. Cui, Sulfiphilic nickel phosphosulfide enabled Li_2S impregnation in 3D graphene cages for Li–S batteries, Adv. Mater. 29 (2017) 1603366.
[6] M. Xiang, H. Wu, H. Liu, J. Huang, Y. Zheng, L. Yang, P. Jing, Y. Zhang, S. Dou, H. Liu, A flexible 3D multifunctional MgO-decorated carbon Foam@CNTs hybrid as self-supported cathode for high-performance lithium-sulfur batteries, Adv. Funct. Mater. 27 (2017) 1702573.
[7] Q. Zhu, Q. Zhao, Y. An, B. Anasori, H. Wang, B. Xu, Ultra-microporous carbons encapsulate small sulfur molecules for high performance lithium-sulfur battery, Nano Energy 33 (2017) 402–409.
[8] C. Tang, B.Q. Li, Q. Zhang, L. Zhu, H.F. Wang, J.L. Shi, F. Wei, CaO-Templated growth of hierarchical porous graphene for high-power lithium–sulfur battery applications, Adv. Funct. Mater. 26 (2016) 577–585.
[9] X. Fang, W. Weng, J. Ren, H. Peng, A cable-shaped lithium sulfur battery, Adv. Mater. 28 (2016) 491–496.
[10] H.J. Peng, J.Q. Huang, X.B. Cheng, Q. Zhang, Review on high-loading and high-energy lithium–sulfur batteries, Adv. Energy Mater. 7 (2017) 1700260.
[11] C. Wang, K. Su, W. Wan, H. Guo, H. Zhou, J. Chen, X. Zhang, Y. Huan, High sulfur loading composite wrapped by 3D nitrogen-doped graphene as a cathode material for lithium–sulfur batteries, J. Mater. Chem. 2 (2014) 5018–5023.
[12] Y. You, W. Zeng, Y.X. Yin, J. Zhang, C.P. Yang, Y. Zhu, Y.G. Guo, Hierarchically micro/mesoporous activated graphene with a large surface area for high sulfur loading in Li–S batteries, J. Mater. Chem. 3 (2015) 4799–4802.
[13] S.H. Chung, C.H. Chang, A. Manthiram, Hierarchical sulfur electrodes as a testing platform for understanding the high-loading capability of Li-S batteries, J. Power Sources 334 (2016) 179–190.
[14] S.S. Zhang, D.T. Tran, A proof-of-concept lithium/sulfur liquid battery with exceptionally high capacity density, J. Power Sources 211 (2012) 169–172.
[15] L. Hu, F. La Mantia, H. Wu, X. Xie, J. McDonough, M. Pasta, Y. Cui, Lithium-ion textile batteries with large areal mass loading, Adv. Energy Mater. 1 (2011) 1012–1017.
[16] C.N. Lin, W.C. Chen, Y.F. Song, C.C. Wang, L.D. Tsai, N.L. Wu, Understanding dynamics of polysulfide dissolution and re-deposition in working lithiumesulfur battery by in-operando transmission X-ray microscopy, J. Power Sources 263 (2014) 98–103.
[17] Y. Li, K.K. Fu, C. Chen, W. Luo, T. Gao, S. Xu, J. Dai, G. Pastel, Y. Wang, B. Liu, J. Song, Y. Chen, C. Yang, L. Hu, Enabling high-areal-capacity lithium–sulfur batteries: designing anisotropic and low-tortuosity porous architectures, ACS Nano 11 (2017) 4801–4807.
[18] X.X. Peng, Y.Q. Lu, L.L. Zhou, T. Sheng, S.Y. Shen, H.G. Liao, L. Huang, J.T. Li, S. G. Sun, Graphitized porous carbon materials with high sulfur loading for lithium-sulfur batteries, Nano Energy 32 (2017) 503–510.
[19] X.B. Cheng, J.Q. Huang, Q. Zhang, H.J. Peng, M.Q. Zhao, F. Wei, Aligned carbon nanotube/sulfur composite cathodes with high sulfur content for lithium–sulfur batteries, Nano Energy 4 (2014) 65–72.
[20] W.C. Du, Y.X. Yin, X.X. Zeng, J.L. Shi, S.F. Zhang, L.J. Wan, Y.G. Guo, Wet chemistry synthesis of multidimensional nanocarbon–sulfur hybrid materials with ultrahigh sulfur loading for lithium–sulfur batteries, ACS Appl. Mater. Interfaces 8 (2016) 3584–3590.
[21] F. Pei, L. Lin, D. Ou, Z. Zheng, S. Mo, X. Fang, N. Zheng, Self-supporting sulfur cathodes enabled by two-dimensional carbon yolk-shell nanosheets for high-energy-density lithium-sulfur batteries, Nat. Commun. 8 (2017) 482.
[22] C. Luo, W. Lv, Y. Deng, G. Zhou, Z.Z. Pan, S. Niu, B. Li, F. Kang, Q.H. Yang, A dual-function Na_2SO_4 template directed formation of cathode materials with a high content of sulfur nanodots for lithium–sulfur batteries, Small 13 (2017) 1700358.

[23] G. Li, J. Sun, W. Hou, S. Jiang, Y. Huang, J. Geng, Three-dimensional porous carbon composites containing high sulfur nanoparticle content for high-performance lithium–sulfur batteries, Nat. Commun. 7 (2016) 10601.
[24] L.X. Miao, W.K. Wang, A.B. Wang, K.G. Yuan, Yu-Sheng Yang, A high sulfur content composite with core–shell structure as cathode material for Li–S batteries, J. Mater. Chem. 1 (2013) 11659–11664.
[25] J.P. Perdew, K. Burke, M. Ernzerhof, Generalized gradient approximation made simple, Phys. Rev. Lett. 77 (1996) 3865–3868.
[26] G. Kresse, J. Hafner, Ab initio molecular dynamics for liquid metals, Phys. Rev. B Condens. Matter Mater. Phys. 47 (1993) 558–561.
[27] P. Goswami, M. Basak, Sulfur Dye in Kirk-Othmer Encyclopedia of Chemical Technology, John Wiley & Sons, 2014.
[28] G. Zhou, H. Tian, Y. Jin, X. Tao, B. Liu, R. Zhang, Z.W. Seh, D. Zhuo, Y. Liu, J. Sun, J. Zhao, C. Zu, D.S. Wu, Q. Zhang, Yi Cui, Catalytic oxidation of Li_2S on the surface of metal sulfides for Li−S batteries, Proc. Natl. Acad. Sci. 114 (2017) 840–845.
[29] L. Ma, H. Zhuang, S. Wei, K.E. Hendrickson, M.S. Kim, G. Cohn, R.G. Hennig, L. A. Archer, Enhanced Li–S batteries using amine-functionalized carbon nanotubes in the cathode, ACS Nano 10 (2016) 1050–1059.